



Chirality-Induced Giant Unidirectional Magnetoresistance in Twisted Bilayer Graphene

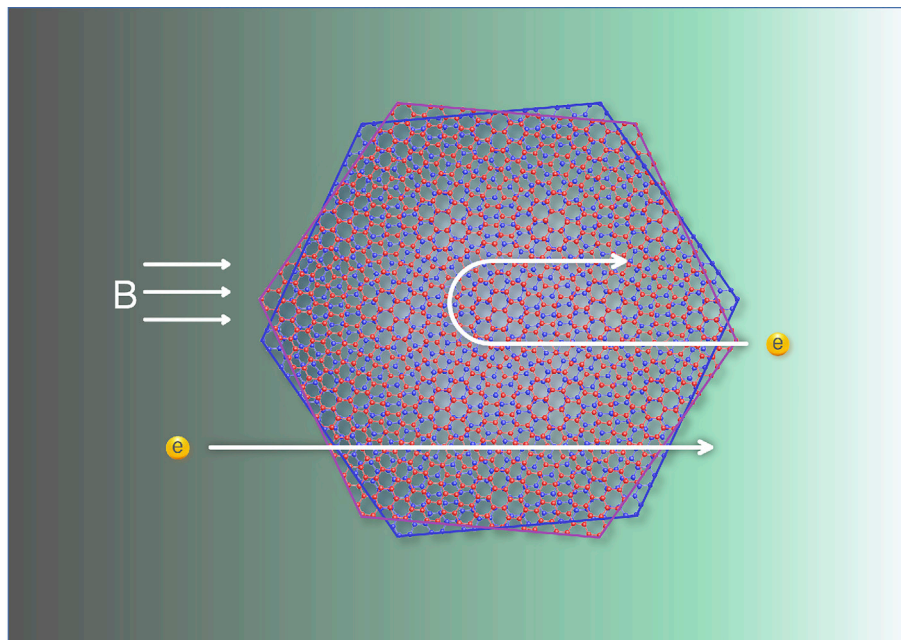
Yizhou Liu,¹ Tobias Holder,¹ and Binghai Yan^{1,*}

*Correspondence: binghai.yan@weizmann.ac.il

Received: November 9, 2020; Accepted: January 18, 2021; Published Online: January 21, 2021; <https://doi.org/10.1016/j.xinn.2021.100085>

© 2021 The Authors. This is an open access article under the CC BY-NC-ND license (<http://creativecommons.org/licenses/by-nc-nd/4.0/>).

GRAPHICAL ABSTRACT



PUBLIC SUMMARY

- Twisted bilayer graphene (TBG) was recently discovered to exhibit fascinating phenomena like the superconductivity and Mott insulating state
- TBG's chirality leads to a unidirectional magnetoresistance (UMR), where magnetoresistance is lower in a chirality-dependent direction. The flat bands of TBG enhance the UMR dramatically
- The giant UMR represents diode-like current rectification and can convert radiation (e.g., terahertz) into currents for energy-harvesting and photodetection



Chirality-Induced Giant Unidirectional Magnetoresistance in Twisted Bilayer Graphene

Yizhou Liu,¹ Tobias Holder,¹ and Binghai Yan^{1,*}

¹Department of Condensed Matter Physics, Weizmann Institute of Science, Rehovot 76100, Israel

*Correspondence: binghai.yan@weizmann.ac.il

Received: November 9, 2020; Accepted: January 18, 2021; Published Online: January 21, 2021; <https://doi.org/10.1016/j.xinn.2021.100085>

© 2021 The Authors. This is an open access article under the CC BY-NC-ND license (<http://creativecommons.org/licenses/by-nc-nd/4.0/>).

Citation: Liu Y., Holder T., and Yan B. (2021). Chirality-Induced Giant Unidirectional Magnetoresistance in Twisted Bilayer Graphene. *The Innovation* 2(1), 100085.

Twisted bilayer graphene (TBG) exhibits fascinating correlation-driven phenomena like the superconductivity and Mott insulating state, with flat bands and a chiral lattice structure. We find by quantum-transport calculations that the chirality leads to a giant unidirectional magnetoresistance (UMR) in TBG, where the unidirectionality refers to the resistance change under the reversal of the direction of current or magnetic field. We point out that flat bands significantly enhance this effect. The UMR increases quickly upon reducing the twist angle, and reaches about 20% for an angle of 1.5° in a 10 T in-plane magnetic field. We propose the band structure topology (asymmetry), which leads to a direction-sensitive mean free path, as a useful way to anticipate the UMR effect. The UMR provides a probe for chirality and band flatness in the twisted bilayers.

KEYWORDS: twisted bilayer graphene; unidirectional magnetoresistance; nonreciprocal transport; chirality; flat bands; topology; nonlinear phenomena

INTRODUCTION

Twisted bilayer graphene (TBG) with a small interlayer angle forms a chiral moiré superlattice, whose superlattice minibands exhibit greatly reduced velocity.^{1–3} The flat bands at the magic angle near 1° provide an ideal platform to study correlation-driven phenomena^{4–16}, for example, unconventional superconductivity and the Mott insulating state. TBG has also motivated the design of twisted structures of other van der Waals materials.^{17–28} In contrast, chirality-induced transport phenomena are less explored thus far.^{29–32}

The chirality and flat bands motivate us to investigate the electric magnetochiral anisotropy (EMCA),³³ which is characterized by the unidirectional magnetoresistance (UMR) in twisted bilayer systems. In an ordinary material, the resistance remains the same upon reversing the direction of the current or the magnetic field. In a chiral system, however, the magnetoresistance (MR) is nonreciprocal, and the chirality determines the preferred direction of the UMR. We note that the EMCA is different from the known anisotropic magnetoresistance (AMR), which remains the same when reversing the magnetic field direction. The EMCA was observed, for example, in Bismuth helices,³³ DNA,^{34,35} and other quantum materials,³⁶ in which the relative amplitude of UMR was usually several percent. Very recent experiments based on the quantum spin Hall edges³⁷ and quantum anomalous Hall edges³⁸ reported giant UMR (according to the definition of Equation 4) of 33% and 13%, respectively. This large UMR promises applications in optoelectronic and spintronic devices. The UMR represents a current rectification, which can generate a DC current in an AC electric field and can be controlled by the magnetic field. This rectification effect can be used for photon-detection or energy-harvesting from long-wavelength light. The dependence of the UMR on the direction and amplitude of the magnetic field provides a sensor for the vector magnetic field.

Different from ordinary transport experiments, the UMR measurement probes the symmetry-breaking and dissipative process such as magnetic excitations.³⁹ It is commonly attributed to the inelastic scattering by magnons⁴⁰ or spin clusters.⁴¹ However, it is unclear how the intrinsic band structure acts

in UMR. Especially for the twisted bilayers, it is an interesting question which role flat bands play for the UMR.

In this work, we find that flat bands generally induce a large UMR for TBG through the orbital effect in an in-plane magnetic field. Our quantum-transport calculations demonstrate an increasing UMR when reducing the twist angle down to the magic angle. The two-terminal MR non-reciprocity is determined by two factors: different electron velocities along counter-propagating directions, and the dephasing in the transport. With these two ingredients, we derive a formula to estimate the UMR from the band structure, which agrees quantitatively with our calculations within the Landauer-Büttiker formalism. Here, the magnetic field induces direction-dependent Fermi velocities in the band structure and thus leads to a direction-dependent mean free path, resulting in the UMR effect. The UMR is inversely proportional to the Fermi velocity and thus strongly enhanced by flat bands. It can reach about 20% for smaller twist angle 1.5° in an in-plane magnetic field of 10 T. Because the UMR effect originates in the symmetry-breaking (both time-reversal- and inversion-breaking), it can exist even if strong electron-electron interactions renormalize the band structure.

RESULTS

The TBG belongs to the chiral point group D_6 , which exhibits no inversion or mirror symmetry. In a system with either inversion symmetry (or the 2-fold rotation around the z axis for a 2D material) or time-reversal symmetry, the left- and right-moving electrons have the same velocity at the Fermi surface. If both inversion and time-reversal symmetry are broken, the left and right movers exhibit different Fermi velocities, as illustrated in Figure 1. This is the case for chiral TBG in an in-plane magnetic field. The velocity imbalance leads to the UMR, as we will discuss in the following. In contrast, the out-of-plane field, which preserves the 2-fold rotation around z, requires further symmetry reductions to break the band structure symmetry of TBG.

We first demonstrate the UMR effect by a phenomenological model. Suppose a two-terminal device with the scattering region of length L , whose conductance can be evaluated as⁴⁷

$$G_0 = G_B \frac{\lambda}{\lambda + L}, \quad (\text{Equation 1})$$

where G_B is the ballistic conductance and λ is the phase-coherent length or the mean free path. Equation (1) connects the ballistic and diffusive limits, which correspond to $\lambda \gg L$ and $\lambda \ll L$, respectively. For a finite dephasing parameter η , $\lambda_{\rightarrow/\leftarrow} = v_{\rightarrow/\leftarrow} \hbar / \eta$ where $v_{\rightarrow/\leftarrow}$ is the right/left-moving Fermi velocity. We generalize Equation 1 to evaluate the conductance (G_{\rightarrow}) and resistance (R_{\rightarrow}) from the left to the right as

$$G_{\rightarrow} = G_B \left(1 + \frac{\eta L}{\hbar v_{\rightarrow}} \right)^{-1}, \quad (\text{Equation 2})$$

$$R_{\rightarrow} = R_B \left(1 + \frac{\eta L}{\hbar v_{\rightarrow}} \right), \quad (\text{Equation 3})$$

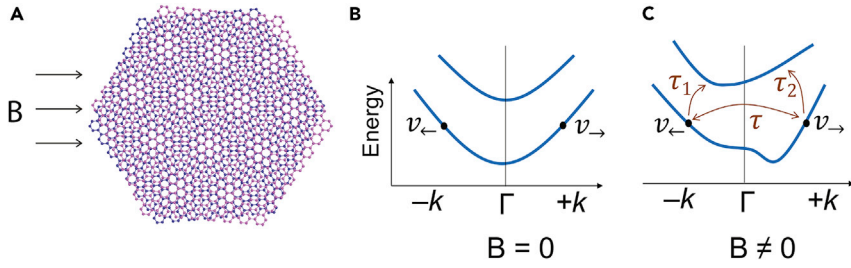


Figure 1. The chiral structure of TBG and illustration of the band structure asymmetry (A) The lattice structure of a TBG. The red and blue spheres represent carbon atoms in the top and bottom layers, respectively. The TBG belongs to the chiral point group D_6 . (B and C) Schematics of the band symmetry-breaking of a chiral system induced by the magnetic field (**B**). (B) Without the magnetic field, the left- and right-moving electrons have the same velocity ($v_{\leftarrow} = v_{\rightarrow}$) at generic Fermi energy. Corresponding left- and right-moving conductance are equal, $G_{\leftarrow} = G_{\rightarrow}$. (C) If finite **B** breaks the time-reversal symmetry, the velocity balance is violated ($v_{\leftarrow} > v_{\rightarrow}$). Thus, the conductance becomes nonreciprocal, i.e., $G_{\leftarrow}(\mathbf{B}) > G_{\rightarrow}(\mathbf{B})$, according to Equation 2. The red arrows indicate the principle of how micro-nonreversibility happens.

Based on Fermi's Golden rule the ordinary relaxation rate τ between each other enforces the microreversibility i.e. $\tau_{\leftarrow} = \tau_{\rightarrow}$. However, the nonreciprocity can exist when second relaxation channels (τ_1 and τ_2) are taken into account.

where G_B is the ballistic conductance and $R_B \equiv 1/G_B$. At finite η , the directional conductance or resistance depends on the corresponding Fermi velocity. Equations 2 and 3 give an intuitive explanation of a mechanism for the UMR. They also provide an alternative way to quantitatively estimate the unidirectional conductance from the band structure of a mesoscopic system.

The UMR can further be justified in a semiclassical picture where the left- and right-moving electrons scatter mostly between each other within the same band. But there is additionally some weak scattering into states provided by a nearby band. This side-channel of relaxation leads to an additional resistance with a coefficient that depends on the density of states (DOS) ($\tau_{\leftarrow} \neq \tau_{\rightarrow}$), yielding Equation 2 (see more in the Supplemental Information). Therefore, if $v_{\rightarrow} > v_{\leftarrow}$ (Figure 1C), this yields nonreciprocal transport with $G_{\rightarrow} > G_{\leftarrow}$ or $R_{\rightarrow} < R_{\leftarrow}$. We assume that the dephasing in both directions is equal. In addition, Ideue et al.⁴⁹ discussed the band structure asymmetry to induce the nonreciprocal transport in the diffusive regime described by the second-order Boltzmann equation.

Furthermore, we find that flat bands can generally enhance the UMR because

$$\frac{\Delta R}{R} = \frac{R_{\rightarrow} - R_{\leftarrow}}{R_{\rightarrow} + R_{\leftarrow}} = \frac{-\Delta G}{G} \quad (\text{Equation 4})$$

$$= \frac{v_{\leftarrow} - v_{\rightarrow}}{\frac{2\hbar v_{\leftarrow} v_{\rightarrow}}{\eta L} + v_{\rightarrow} + v_{\leftarrow}} \quad (\text{Equation 5})$$

$$\eta L \gg \infty \frac{v_{\leftarrow} - v_{\rightarrow}}{v_{\rightarrow} + v_{\leftarrow}} \propto (v_{\leftarrow} - v_{\rightarrow}) \cdot \text{DOS}. \quad (\text{Equation 6})$$

Equation 6 indicates that the upper limit of the UMR is an intrinsic quantity determined by the field-modified band structure, non-withstanding the fact that it requires finite dephasing/dissipation. The term $1/(v_{\rightarrow} + v_{\leftarrow})$ in Equation 6 represents the DOS, and thus the amplitude of the UMR is approximately proportional to the DOS. In addition, the velocity imbalance requires breaking of both the inversion symmetry and time-reversal symmetry. The time-reversal breaking can be realized by an external magnetic field or spontaneous magnetization in TBG.^{6,7} It should be noted that Equations 5 and 6 are only accurate for the single-mode case at the Fermi energy. The ηL dependence of the UMR can be nonmonotonic in the many-band case (see the Supplemental Information for more details). On the other hand, we do not expect qualitative changes to the phenomenology in the presence of strong electron-electron interactions, which to a large extent preserve momenta and thus influence transport only indirectly.

Magneto-chiral effect of TBG. —In the presence of an in-plane magnetic field (**B**), the symmetry-allowed corrections to the resistance/conductance of the current **I** are in the form of $\mathbf{I} \cdot \mathbf{B}$ and $\mathbf{I} \times \mathbf{B}$. They satisfy the global Onsager's reciprocal relation⁵⁰, i.e., $R(\mathbf{I}, \mathbf{B}) = R(-\mathbf{I}, -\mathbf{B})$. The resistance in EMCA is usually written as^{33,51}

$$R(\mathbf{I}, \mathbf{B}) = R_0 + \chi^{L,R} \mathbf{I} \cdot \mathbf{B} + \gamma (\mathbf{I} \times \mathbf{B}) \cdot \mathbf{P} + \beta \mathbf{B}^2, \quad (\text{Equation 7})$$

where $\chi^{L,R}$ represents the chirality with $\chi^L = -\chi^R$, γ and β are constants, and **P** the charge polarization. The last \mathbf{B}^2 term represents the ordinary MR due to the Lorentz force, which is reciprocal.

Equation 7 indicates the nonlinear I-V dependence and the second-harmonic resistance induced by an AC electric field. We point out that the dephasing term η in nonequilibrium Green's function (NEGF) calculations or Equations 2 and 3 includes both elastic and inelastic scattering. The inelastic scattering leads to the nonlinear effects.

In TBG, the chirality refers to the twisted direction, left- or right-handed. In the device, the h-BN substrate induces the sublattice symmetry-breaking,^{52–57} reducing the D_6 symmetry to C_3 and leading to an out-of-plane dipole. The in-plane strain can further break the C_3 rotation to C_1 ^{11,12} and induces an in-plane dipole. For the D_6 symmetry, the chiral term $\mathbf{I} \cdot \mathbf{B}$ contributes to the magneto-transport. For the case of C_3 symmetry, the additional dipole term $(\mathbf{I} \times \mathbf{B}) \cdot \mathbf{P}$ emerges. We will focus on these two terms in the following and later discuss the C_1 case with the in-plane dipole. It is convenient to calculate the conductance, compared with the resistance, with the NEGF method. Thus, in the following, we evaluate the unidirectional magneto-conductance (UMC).

First, we take TBG with the twist angle $\theta = 3.15^\circ$ to demonstrate the UMC for both cases, $\mathbf{B} \parallel \mathbf{I}$ and $\mathbf{B} \perp \mathbf{I}$. We calculate the conductance change $\Delta G = G_{\rightarrow}(\mathbf{B}) - G_{\leftarrow}(\mathbf{B})$ through a TBG nanoribbon by NEGF. The outer section of the nanoribbon is used as two leads in the device, as shown in Figure 2A. The applied magnetic field $\mathbf{B} \parallel \mathbf{I}$ leads to a phase in the interlayer hopping and breaks the velocity balance at opposite k , a consequence of time-reversal breaking. This $k \rightarrow -k$ symmetry breaking is shown in the band structure in Figure 2B. To demonstrate the band structure change and ΔG clearly, we apply a large magnetic field 50 T for this twist angle.

Subsequently, UMC emerges with nonzero ΔG . The peaks of ΔG originate from band edges where the velocity approaches zero and the DOS exhibits a peak, consistent with the prediction of Equation 2. We point out that ΔG depends on the dephasing parameter η . If $\eta = 0$, which represents fully coherent transport, we obtain $\Delta G = 0$ in the NEGF calculations and also according to Equation 2. The opposite limit $\eta \rightarrow \infty$ also yields $\Delta G \rightarrow 0$, because electrons do not remember their group velocity in the diffusive limit without any coherence. A large ΔG appears in the intermediate region (see Figures 2C and 2D), where the finite η violates the charge conservation in the two-terminal conductance because it effectively introduces a non-Hermitian term $i\eta$ into the Hamiltonian thus breaking the probability conservation of Schrödinger equation.⁴⁸ Therefore, the existence of a two-terminal UMC/UMR requires both dephasing and partial coherence, which can be induced by the inelastic scattering.

Next, we rotate the magnetic field as $\mathbf{B} \perp \mathbf{I}$. We further induce an electric dipole **P** out of the plane by adding a potential difference ΔU between both layers (see Figure 2E). Then, a UMC emerges due to the $(\mathbf{B} \times \mathbf{I}) \cdot \mathbf{P}$ term in Equation 7. The value of ΔG is approximately proportional to the potential ΔU and also relies on a finite η . Similar to the case $\mathbf{B} \parallel \mathbf{I}$, the band edges constitute the peaks in ΔG .

We stress that Equation 2 agrees quantitatively with the NEGF calculations especially in the small η regime, as demonstrated in Figures 2C, 2D, and 2G.

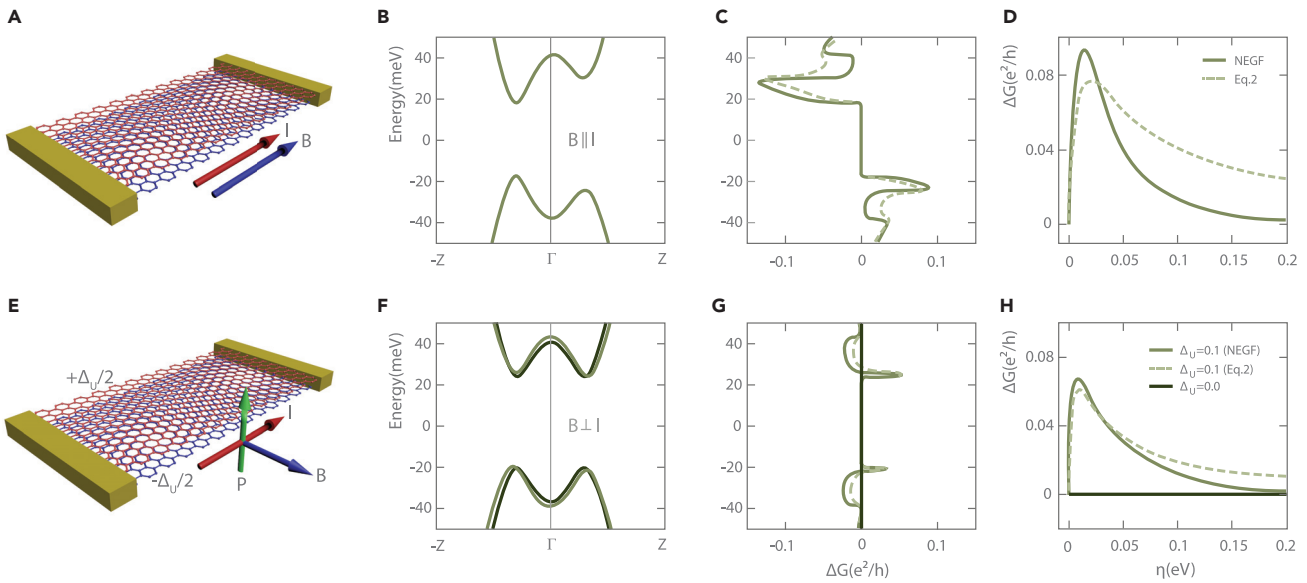


Figure 2. The band structure and conductance of TBG with twisted angle 3.15° (A) Schematic of the transport device of TBG under in-plane magnetic field $\mathbf{B}||\mathbf{I}$. (B) The band structure for the nanoribbon (the device region in a) with $B = 50$ T. (C) The direction-induced conductance change $\Delta G = G_+ - G_-$ at different Fermi energies. Results from the NEGF method and Equation 2 agree very well. The conductance is calculated with a constant dephasing parameter $\eta = 0.01$ eV. (D) The peak value of ΔG for the valence band top depends non-monotonically on the dephasing parameter η . The NEGF and Equation 2 provides similar results, especially in the small η regime. (E) The device for $\mathbf{B} \perp \mathbf{I} \perp \mathbf{P}$. \mathbf{P} is the charge dipole induced by the parameter Δ_U . (F) Corresponding band structures for $\Delta_U = 0, 0.1$ eV. The applied magnetic field is $B = 50$ T. (G) Corresponding ΔG at different Fermi energies. (H) The η -dependence of ΔG . Solid curves are calculated by NEGF and the dashed one is evaluated from Equation 2.

The deviation in the regime of large η is likely because Equation 2 neglects interference effects.⁵⁸ Such effects come into play once further relaxation processes are taken into account for the electrons that are already relaxed via the side-channel. However, these processes are higher order not only in terms of η but also microscopically in terms of processes that lead to a finite η . Therefore, to evaluate the UMC for smaller twist angles where the NEGF demands much more computational time, we will use Equation 2 without sacrificing much accuracy.

The nanoribbon configuration indicates that the flatness of the band edges leads to a large UMC. However, the finite width (e.g., one moiré unit in Figure 2)

and the existence of edge states implies that the ribbon configuration can exhibit different transport behavior from the extended 2D bilayer. For this reason, we investigate in the following a sheet of TBG with infinite width for several twist angles. To this end, the UMC is extracted by summing the 1D conductance (Equation 2) over the transverse momenta.

As the twist angle decreases, the band dispersion turns flat in the low-energy regime (see SM). Figure 3 shows the band structure and the UMC for 2D TBG with $\theta = 1.5^\circ$. In both the $\mathbf{B}||\mathbf{I}$ and $\mathbf{B} \perp \mathbf{I}$ cases, the UMC ($\Delta\sigma_{xx}/\sigma_{xx}$) is larger in the flat band window (-30 to 30 meV in Figure 3A) between the single-particle gaps, and one order of magnitude smaller in the regime of more

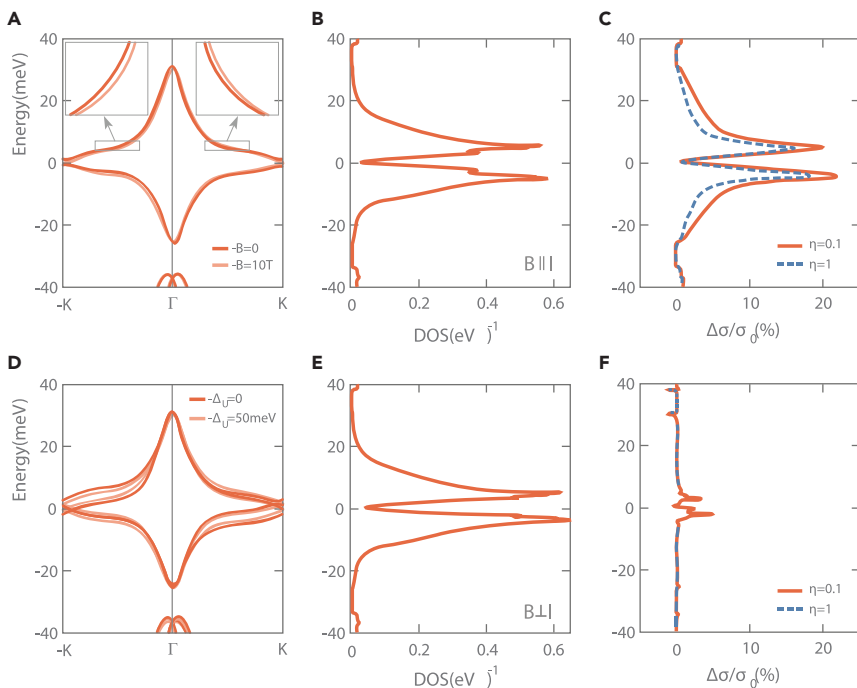


Figure 3. Band structure and UMR of the TBG with $\theta = 1.5^\circ$ for $\mathbf{I} || \mathbf{B}$ (A–C) and $\mathbf{I} \perp \mathbf{B}$ (D–F) (A and D) The band structure along high-symmetry lines. For $\mathbf{I} || \mathbf{B}$ black (red) lines represent the results for $B = 10$ ($B = 0$) T; for $\mathbf{I} \perp \mathbf{B}$ they represent results for $\Delta_U = 0$ ($\Delta_U = 50$) meV with fixed magnetic field $B = 10$ T. The Fermi energy is set to zero, i.e., the charge neutral point. (B and E) DOS under the magnetic field. (C and F) Calculated UMC ($\Delta\sigma_{xx}/\sigma_{xx}$). Black solid and blue dashed lines represent $\eta = 1$ and 0.1 meV, respectively.

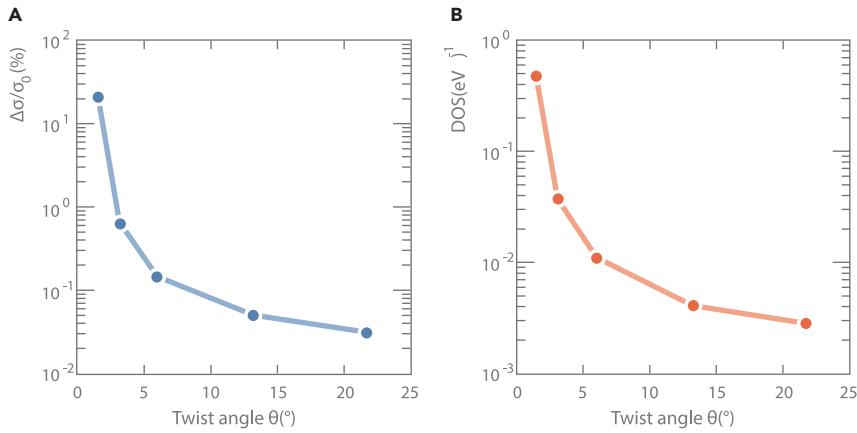


Figure 4. UMC and DOS The two-terminal (2T) UMC calculated by Equation 5 (A) and DOS (B) at peak position right below the charge neutral point for TBG at different angles. The UMC is approximately proportional to the DOS which agrees with Equation 6.

dispersive band. For $\mathbf{B} \parallel \mathbf{I}$, large UMC peaks up to 22% exists at the same energies (about ± 10 meV) as the DOS peaks, which are caused by the saddle points of flat bands. The UMC is also large near the band edge and diminishes quickly in higher energies for the dispersive bands. One can see that regions close to a van Hove singularity, i.e., saddle points and band edges, contribute substantially to the UMC. As shown in Figure 3D, as the product ηL increases from zero, one can find that the UMC increases fast until it quickly reaches the peak value. For L in the μm size, $\Delta\sigma_{xx}/\sigma_{xx}$ reaches the peak value for η in the order of 0.1 meV, which corresponds to a picoseconds lifetime. In experiment, L is usually several μm and $\eta \sim 1$ meV (e.g., in Yuan et al.,⁴ the lifetime is ~ 0.1 ps).

The chirality-induced UMC/UMR increases quickly when the bands become flatter upon reducing θ . Figure 4A shows the θ -dependence of the UMC peak value slightly below the charge neutral point (see the energy dependence in SM). The UMC peaks are proportional to corresponding DOS peaks (Figure 4B) at different θ , well consistent with the observation from Equation 6.

For $\mathbf{B} \perp \mathbf{I}$, we add a $\Delta U = 50$ meV potential difference to create a polarization \mathbf{P} along the z axis, leading to the $(\mathbf{B} \times \mathbf{I}) \cdot \mathbf{P}$ term for UMC/UMR. The UMC exhibits also large peaks in the flat band regime and at band edges of the dispersive bands. Two peaks below and above the charge neutral point are

rather asymmetric compared to those in the $\mathbf{B} \parallel \mathbf{I}$ case, which is related to the asymmetry in the DOS (Figure 3E).

DISCUSSION

Although we discussed the UMR effect in a two-terminal setup, UMR can exist in multiple terminal devices, in which the UMR may even become stronger. In fact, devices with multiple terminals are commonly used in experiments^{4,5}. In two-terminal transport, the UMR requires a finite η to act as a virtual lead which breaks charge conservation.^{35,48} In cases with multiple terminals, charges can naturally leak to other leads. For example, Figure 5B shows a three-terminal device for TBG with $\theta = 21.8^\circ$. The three-terminal UMC is less sensitive to η and two orders of magnitude larger than the two-terminal result (Figures 5C and 5D). We note that smaller angles show the same trend (see Figure S5). Therefore, we expect the UMR to be even larger in multiple terminal experiments than in the above two-terminal results.

The current dependence of the resistance in Equation 7 indicates a nonlinear phenomenon. In an experiment with an AC electric field, the UMR can be extracted from the second-harmonic resistance $R_{xx}^{(2\omega)}$ ^{37,38,59}. For an angle φ between the in-plane field \mathbf{B} and the current \mathbf{I} , the resistance has an elliptical dependence of the form $\alpha \cos\varphi + \beta \sin\varphi$, where α, β are parameters. This dependence is dissimilar to the case of

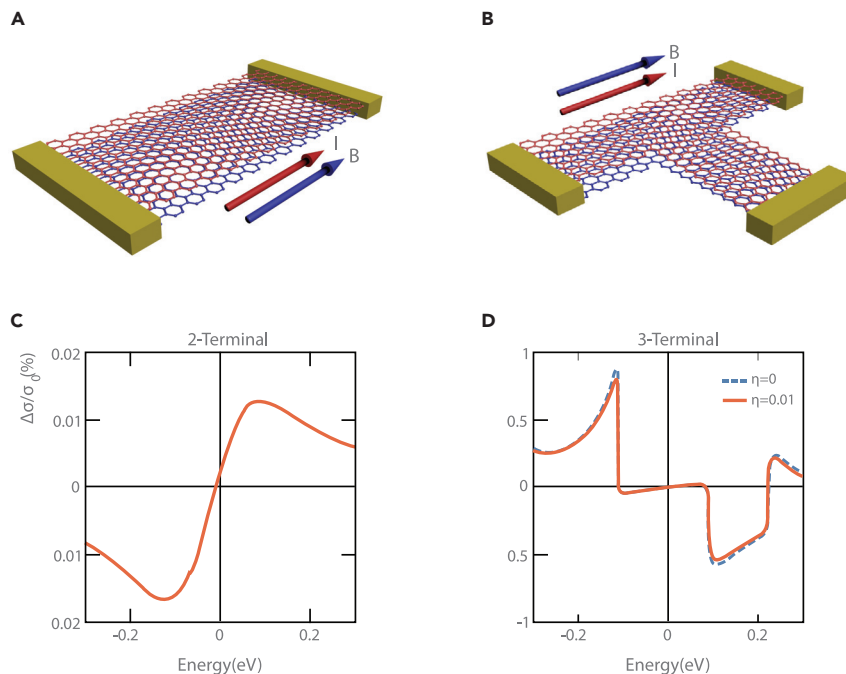


Figure 5. Three-terminal (3T) transport (A and B) Schematics of 2T and 3T devices. (C and D) Comparison of the 2T and 3T UMR calculated by NEGF method for $\mathbf{B} \parallel \mathbf{I}$ and $B = 10$ T. For the 2T device, a finite dephasing parameter $\eta = 10$ meV is used; for the 3T one, both $\eta = 0$ (red) and 10 meV (blue) are examined.

AMR, which has the form of $\sin 2\varphi$. Therefore, while in the experiment both UMR and AMR may coexist, they can be disentangled by the periodicity in the angular dependence.

As discussed above, UMR is sensitive to the symmetry of the TBG. In the ideal D_6 symmetry case, UMR exists only for $\mathbf{B} \parallel \mathbf{l}$. In the C_3 case with interlayer potential difference, UMR appears also for $\mathbf{B} \perp \mathbf{l}$ where \mathbf{B} is still in-plane. In the lowest symmetry case C_1 with possible in-plane strain, UMR further allows for the out-of-plane \mathbf{B} field, where, however, the ordinary B^2 term is usually overwhelming.

The nonreciprocal transport was recently found to be strongly enhanced by superconductivity in chiral or noncentrosymmetric superconductors.^{60–62} It will be intriguing to investigate the UMR effect in the presence of superconductivity for TBG. Furthermore, in experiment magic-angle TBG can exhibit orbital ferromagnetism^{6–8,14,63–65} due to the electron-electron interaction.^{30,56,66–70} We point out that the orbital magnetism also leads to UMR where it plays the same role as the magnetic field. The orbital moment may modify the band structure much stronger than the magnetic field, inducing even larger UMR if the two-fold out-of-plane rotational symmetry is further broken by lattice strain or substrate effects.

In summary, we report the giant UMR in TBG as an orbital-derived phenomenon in the magnetic field. The UMR originates in the chiral atomic structure and gets enhanced by flat bands. We argue that the predicted UMR should be detectable in current experimental conditions. Besides quantum-transport calculations, we derived simple formulas (Equations 2 and 3) to monitor the UMR effect from the band structure, which is based on the direction-sensitive mean free path. Although the UMR is dependent on the dephasing and device geometry, it approaches a finite value in the strong scattering limit. This UMR limit is an intrinsic material quantity that depends on Fermi velocities of the band structure. Thus, the UMR provides a direct probe to the flatness of the dispersion. In addition, our findings for TBG can be generalized to other chiral twisted bilayers and chiral crystals.

MATERIALS AND METHODS

We adopt the tight-binding Hamiltonian to describe the band structure of TBG outlined in Moon and Koshino.⁴² This tight-binding model includes all atomic sites of two layers and is compatible with the introduction of an in-plane magnetic field. We consider the orbital effect of the magnetic field $\mathbf{B} = (B_x, B_y, 0)$ and ignore the weak spin splitting and negligible spin-orbit interaction. Suppose a two-terminal device where the current flows along the x direction. We choose the gauge $\mathbf{A} = (B_y z, -B_x z, 0)$ so that the lattice translational symmetry along x (the charge current direction) is still preserved. The modification of the hopping integrals by the magnetic field is taken into account via a Peierls substitution.^{43,44} Because it promotes the inversion symmetry and loses the chiral character, we do not employ the Bistritzer-MacDonald¹ continuum model for TBG even though it can easily include an in-plane magnetic field.^{45,46}

To evaluate the UMR, we calculate the total conductance of a two-terminal device with an in-plane magnetic field by the NEGF method.⁴⁷ The whole system is divided into three parts: two semi-infinite reservoirs acting as electron leads, and a scattering region connecting them. We set these three parts as the same TBG ribbons along the x direction, which preserve the D_6 point group symmetry (cf. Figure 2A). The conductance from lead q to p is $G_{p \rightarrow q} = \text{Tr}(\Gamma_p \mathcal{G} \Gamma_q \mathcal{G}^\dagger)$ where $\Gamma_{p(q)} = i(\Sigma_{p(q)} - \Sigma_{p(q)}^\dagger)$ is the anti-Hermitian part of the retarded self-energy matrix $\Sigma_{p(q)}$ of lead $p(q)$; $\mathcal{G} = (E + i\eta)I - H - \Sigma$ is the Green function of scattering region where I is the identity matrix, H is the Hamiltonian, Σ is the total self-energy from coupling to the leads, and η is the dephasing parameter.⁴⁸ If $\eta = 0$ one can prove the reciprocal relation $G_{p \rightarrow q} = G_{q \rightarrow p}$, regardless of the presence of a magnetic field. This amounts to the fact that in coherent transport, the two-terminal conductance depends only on the total channel number but not on the velocity.⁴⁸ However, a finite η spoils this reciprocity, as we discuss now.

REFERENCES

- Bistritzer, R., and MacDonald, A.H. (2011). Moire bands in twisted double-layer graphene. *Proc. Natl. Acad. Sci. U S A* **108**, 1009.4203. <https://doi.org/10.1073/pnas.1108174108>.
- Lopes dos Santos, J.M.B., Peres, N.M.R., and Castro Neto, A.H. (2007). Graphene bilayer with a twist: electronic structure. *Phys. Rev. Lett.* **99**, 256802.
- Suárez Morell, E., Correa, J.D., Vargas, P., et al. (2010). Flat bands in slightly twisted bilayer graphene: tight-binding calculations. *Phys. Rev. B* **82**, 121407.
- Yuan, C., Valla, F., Demir, A., et al. (2018a). Correlated insulator behaviour at half-filling in magic-angle graphene superlattices. *Nature* **556**, 80–84.
- Cao, Y., Fatemi, V., Fang, S., et al. (2018b). Unconventional superconductivity in magic-angle graphene superlattices. *Nature* **556**, 43–50.
- Sharpe, A.L., Fox, E.J., Barnard, A.W., et al. (2019). Emergent ferromagnetism near three-quarters filling in twisted bilayer graphene. *Science* **365**, 605–608, 1901.03520.
- Serlin, M., Tschirhart, C.L., Polshyn, H., et al. (2019). Intrinsic quantized anomalous Hall effect in a moiré heterostructure. *Science* **367**, 900–903.
- Lu, X., Stepanov, P., Yang, W., et al. (2019). Superconductors, orbital magnets and correlated states in magic-angle bilayer graphene. *Nature* **574**, 653–657, 1903.06513.
- Chen, G., Jiang, L., Wu, S., et al. (2019). Evidence of a gate-tunable Mott insulator in a trilayer graphene moiré superlattice. *Nat. Phys.* **15**, 237–241.
- Jiang, Y., Lai, X., Watanabe, K., et al. (2019). Charge order and broken rotational symmetry in magic-angle twisted bilayer graphene. *Nature* **573**, 91–95.
- Choi, Y., Kemmer, J., Yang, P., et al. (2019). Electronic correlations in twisted bilayer graphene near the magic angle. *Nat. Phys.* **15**, 1174–1180.
- Kerelsky, A., McGilly, L.J., Kennes, D.M., et al. (2019). Maximized electron interactions at the magic angle in twisted bilayer graphene. *Nature* **572**, 95–100.
- Xie, Y., Lian, B., Jack, B., et al. (2019). Spectroscopic signatures of many-body correlations in magic-angle twisted bilayer graphene. *Nature* **572**, 101–105.
- Chen, G., Sharpe, A.L., Fox, E.J., et al. (2020a). Tunable correlated Chern insulator and ferromagnetism in a moiré superlattice. *Nature* **579**, 56–61.
- Zondiner, U., Rozen, A., Rodan-Legrain, D., et al. (2020). Cascade of phase transitions and Dirac revivals in magic-angle graphene. *Nature* **582**, 203–208.
- Wong, D., Nuckolls, K.P., Oh, M., et al. (2020). Cascade of electronic transitions in magic-angle twisted bilayer graphene. *Nature* **582**, 198–202.
- Wu, F., Lovorn, T., Tutuc, E., et al. (2019). Topological insulators in twisted transition metal dichalcogenide homobilayers. *Phys. Rev. Lett.* **122**, 086402.
- Yu, H., Chen, M., and Yao, W. (2019). Giant magnetic field from moiré induced Berry phase in homobilayer semiconductors. *Natl. Sci. Rev.* **7**, 12–20, 1906.05499.
- An, L., Cai, X., Huang, M., et al. (2019). Interaction effects and superconductivity signatures in twisted double-bilayer WSe₂. arXiv, 1907.03966.
- Zhang, Y., Yuan, N.F.Q., and Fu, L. (2019a). Moiré quantum chemistry: charge transfer in transition metal dichalcogenide superlattices. arXiv, 1910.14061.
- Scuri, G., Andersen, T.I., Zhou, Y., et al. (2020). Electrically tunable valley dynamics in twisted WSe₂/WSe₂ bilayers. *Phys. Rev. Lett.* **124**, 217403.
- Pan, H., Wu, F., and Das Sarma, S. (2020). Band topology, Hubbard model, Heisenberg model, and Dzyaloshinskii-Moriya interaction in twisted bilayer WSe₂. arXiv, 2004.04168.
- Merkli, P., Mooshammer, F., Brem, S., et al. (2020). Twist-tailoring Coulomb correlations in van der Waals homobilayers. *Nat. Commun.* **11**, 2167.
- Lian, B., Liu, Z., Zhang, Y., et al. (2020). Flat Chern band from twisted bilayer mnbi₂te₂. *Phys. Rev. Lett.* **124**, 126402.
- Wang, L., Shih, E.-M., Ghiotto, A., et al. (2020). Correlated electronic phases in twisted bilayer transition metal dichalcogenides. *Nat. Mater.* **19**, 861–866.
- Regan, E.C., Wang, D., Jin, C., et al. (2020). Mott and generalized wigner crystal states in wse₂/wse₂ moiré superlattices. *Nature* **579**, 359–363.
- Tang, Y., Li, L., Li, T., et al. (2020). Simulation of hubbard model physics in wse₂/wse₂ moiré superlattices. *Nature* **579**, 353–358.
- Naik, M.H., and Jain, M. (2018). Ultraflatbands and shear solitons in moiré patterns of twisted bilayer transition metal dichalcogenides. *Phys. Rev. Lett.* **121**, 266401.
- Liu, J., and Dai, X. (2020). Anomalous hall effect, magneto-optical properties, and nonlinear optical properties of twisted graphene systems. *NPJ Comput. Mater.* **6**, 1–10.
- He, W.-Y., Goldhaber-Gordon, D., and Law, K.T. (2020). Giant orbital magnetoelectric effect and current-induced magnetization switching in twisted bilayer graphene. *Nat. Commun.* **11**, 1650, 1908.11718.
- Hu, J.-X., Zhang, C.-P., Xie, Y.-M., et al. (2020). Nonlinear hall effects in strained twisted bilayer wse₂. arXiv, 2004.14140.
- Huang, M., Wu, Z., Hu, J., et al. (2020). Giant nonlinear Hall effect in twisted WSe₂. arXiv, 2006.05615.
- Rikken, G.L.J.A., Faling, J., and Wyder, P. (2001). Electrical magnetochiral anisotropy. *Phys. Rev. Lett.* **87**, 236602.
- Xie, Z., Xie, Z., Markus, T.Z., et al. (2011). Spin specific electron conduction through DNA oligomers. *Nano Lett.* **11**, 4652–4655.
- Liu, Y., Xiao, J., Koo, J., et al. (2020). Chirality induced topological nature of electrons in dna-like materials. arXiv, 2008.08881.
- Tokura, Y., and Nagaosa, N. (2018). Nonreciprocal responses from non-centrosymmetric quantum materials. *Nat. Commun.* **9**, 1–14.
- Zhao, W., Fei, Z., Song, T., et al. (2020). Magnetic proximity and nonreciprocal current switching in a monolayer WTe₂ helical edge. *Nat. Mater.* **19**, 503–507.
- Yasuda, K., Morimoto, T., Yoshimi, R., et al. (2020). Large non-reciprocal charge transport mediated by quantum anomalous Hall edge states. *Nat. Nanotechnol.* **15**, 831–835.

39. Yokouchi, T., Kanazawa, N., Kikkawa, A., et al. (2017). Electrical magnetochiral effect induced by chiral spin fluctuations. *Nat. Commun.* **8**, 866, 1703.04897.
40. Yasuda, K., Tsukazaki, A., Yoshimi, R., et al. (2016). Large unidirectional magnetoresistance in a magnetic topological insulator. *Phys. Rev. Lett.* **117**, 127202, 1609.05906.
41. Ishizuka, H., and Nagaosa, N. (2020). Anomalous electrical magnetochiral effect by chiral spin-cluster scattering. *Nat. Commun.* **11**, 2986.
42. Moon, P., and Koshino, M. (2013). Optical absorption in twisted bilayer graphene. *Phys. Rev. B* **87**, 205404.
43. Peierls, R. (1933). Zur theorie des diamagnetismus von leitungselektronen. *Z. Physik* **80**, 763–791.
44. Xiao, D., Chang, M.-C., and Niu, Q. (2010). Berry phase effects on electronic properties. *Rev. Mod. Phys.* **82**, 1959–2007.
45. Kwan, Y.H., Parameswaran, S.A., and Sondhi, S.L. (2020). Twisted bilayer graphene in a parallel magnetic field. *Phys. Rev. B* **101**, 205116.
46. Roy, B., and Yang, K. (2013). Bilayer graphene with parallel magnetic field and twisting: phases and phase transitions in a highly tunable Dirac system. *Phys. Rev. B* **88**, 241107.
47. Datta, S. (2012). *Lessons from Nanoelectronics: A New Perspective on Transport* (World Scientific).
48. Büttiker, M. (1986a). Role of quantum coherence in series resistors. *Phys. Rev. B* **33**, 3020–3026.
49. Ideue, T., Hamamoto, K., Koshikawa, S., et al. (2017). Bulk rectification effect in a polar semiconductor. *Nat. Phys.* **13**, 578–583.
50. Büttiker, M. (1986b). Four-terminal phase-coherent conductance. *Phys. Rev. Lett.* **57**, 1761–1764.
51. Rikken, G.L.J.A., and Wyder, P. (2005). Magnetoelectric anisotropy in diffusive transport. *Phys. Rev. Lett.* **94**, 016601.
52. Jung, J., DaSilva, A.M., MacDonald, A.H., et al. (2015). Origin of band gaps in graphene on hexagonal boron nitride. *Nat. Commun.* **6**, 6308.
53. Hunt, B., Sanchez-Yamagishi, J.D., Young, A.F., et al. (2013). Massive Dirac fermions and Hofstadter butterfly in a van der Waals heterostructure. *Science* **340**, 1427–1430, 1303.6942.
54. Lee, M., Wallbank, J.R., Gallagher, P., et al. (2016). Ballistic miniband conduction in a graphene superlattice. *Science* **353**, 1526–1529.
55. Zhang, Y.-H., Mao, D., and Senthil, T. (2019b). Twisted bilayer graphene aligned with hexagonal boron nitride: anomalous Hall effect and a lattice model. *Phys. Rev. Res.* **1**, <https://doi.org/10.1103/physrevresearch.1.033126>.
56. Bultinck, N., Chatterjee, S., and Zaletel, M.P. (2020). Mechanism for anomalous hall ferromagnetism in twisted bilayer graphene. *Phys. Rev. Lett.* **124**, 166601.
57. Kim, H., Leconte, N., Chittari, B.L., et al. (2018). Accurate gap determination in monolayer and bilayer graphene/h-BN moiré superlattices. *Nano Lett.* **18**, 7732–7741.
58. Baranger, H.U., DiVincenzo, D.P., Jalabert, R.A., et al. (1991). Classical and quantum ballistic-transport anomalies in microjunctions. *Phys. Rev. B* **44**, 10637–10675.
59. Choe, D., Jin, M.-J., Kim, S.-I., et al. (2019). Gate-tunable giant nonreciprocal charge transport in noncentrosymmetric oxide interfaces. *Nat. Commun.* **10**, 4510.
60. Wakatsuki, R., Saito, Y., Hoshino, S., et al. (2017). Nonreciprocal charge transport in noncentrosymmetric superconductors. *Sci. Adv.* **3**, e1602390.
61. Qin, F., Shi, W., Ideue, T., et al. (2017). Superconductivity in a chiral nanotube. *Nat. Commun.* **8**, 14465.
62. Lustikova, J., Shiomi, Y., Yokoi, N., et al. (2018). Vortex rectenna powered by environmental fluctuations. *Nat. Commun.* **9**, 4922.
63. Li, S.-Y., Zhang, Y., Ren, Y.-N., et al. (2020). Experimental evidence for orbital magnetic moments generated by moiré-scale current loops in twisted bilayer graphene. *Phys. Rev. B* **102**, 121406.
64. Chen, S., He, M., Zhang, Y.-H., et al. (2020b). Electrically tunable correlated and topological states in twisted monolayer-bilayer graphene. *arXiv*, 2004.11340.
65. Polshyn, H., Zhu, J., Kumar, M.A., et al. (2020). Nonvolatile switching of magnetic order by electric fields in an orbital Chern insulator. *arXiv*, 2004.11353.
66. Po, H.C., Zou, L., Vishwanath, A., et al. (2018). Origin of mott insulating behavior and superconductivity in twisted bilayer graphene. *Phys. Rev. X* **8**, 031089.
67. Xie, M., and MacDonald, A.H. (2020). Nature of the correlated insulator states in twisted bilayer graphene. *Phys. Rev. Lett.* **124**, 097601.
68. Zhang, Y.-H., Mao, D., and Senthil, T. (2019c). Twisted bilayer graphene aligned with hexagonal boron nitride: anomalous hall effect and a lattice model. *Phys. Rev. Res.* **1**, 033126.
69. Liu, J., and Dai, X. (2019). Spontaneous symmetry breaking and topology in twisted bilayer graphene: the nature of the correlated insulating states and the quantum anomalous Hall effect. *arXiv*, 1911.03760.
70. Wu, F., and Das Sarma, S. (2020). Collective excitations of quantum anomalous hall ferromagnets in twisted bilayer graphene. *Phys. Rev. Lett.* **124**, 046403.

ACKNOWLEDGMENTS

We thank the inspiring discussions with Yuval Oreg, Jiewen Xiao, Shahal Ilani, and Eli Zeldov. B.Y. acknowledges the financial support by the Willner Family Leadership Institute for the Weizmann Institute of Science, the Benozio Endowment Fund for the Advancement of Science, Ruth and Herman Albert Scholars Program for New Scientists, the European Research Council (ERC Consolidator Grant No. 815869, “NonlinearTop”).

AUTHOR CONTRIBUTIONS

B.Y. conceived the project. Y.L. performed the calculations. Y.L., T.H. and B.Y. analyzed the results and wrote the manuscript. All authors reviewed and approved it.

DECLARATION OF INTERESTS

The authors declare that they have no competing interests.

SUPPLEMENTAL INFORMATION

Supplemental Information can be found online at <https://doi.org/10.1016/j.xinn.2021.100085>.

LEAD CONTACT WEBSITE

<http://www.weizmann.ac.il/condmat/Yan/>